Finite-fault slip model of the 2016 M_w 7.5 Chiloé earthquake, southern Chile, estimated from Sentinel-1 data

Wenbin Xu[1] (ID)

[1]Department of Land Surveying and Geo-informatics, The Hong Kong Polytechnic University, Hong Kong, China

Abstract Subduction earthquakes have been widely studied in the Chilean subduction zone, but earthquakes occurring in its southern part have attracted less research interest primarily due to its lower rate of seismic activity. Here I use Sentinel-1 interferometric synthetic aperture radar (InSAR) data and range offset measurements to generate coseismic crustal deformation maps of the 2016 M_w 7.5 Chiloé earthquake in southern Chile. I find a concentrated crustal deformation with ground displacement of approximately 50 cm in the southern part of the Chiloé island. The best fitting fault model shows a pure thrust-fault motion on a shallow dipping plane orienting 4° NNE. The InSAR-determined moment is 2.4×10^{20} Nm with a shear modulus of 30 GPa, equivalent to M_w 7.56, which is slightly lower than the seismic moment. The model shows that the slip did not reach the trench, and it reruptured part of the fault that ruptured in the 1960 M_w 9.5 earthquake. The 2016 event has only released a small portion of the accumulated strain energy on the 1960 rupture zone, suggesting that the seismic hazard of future great earthquakes in southern Chile is high.

1. Introduction

In 1960, the largest-ever earthquake in recorded history, the M_w 9.5 Valdivia earthquake, struck the Nazca-South American subduction zone in southern Chile [*Barrientos and Ward*, 1990; *Bilek*, 2010]. The earthquake ruptured a segment of the megathrust approximately 900 km long, causing significant damage and economic loss [*Barrientos and Ward*, 1990; *Bilek*, 2010]. On 25 December 2016, a large earthquake of M_w 7.5 ruptured the same segment that was ruptured in the 1960 earthquake offshore of Chiloé island [*National Earthquake Information Center (NEIC)*, 2016]. The source region is bound by Chiloé island to the north, the Guaitecas Archipelago to the south, and Guafo island to the west (Figure 1). The U.S. Geological Survey National Earthquake Information Center (USGS-NEIC) determined that the hypocenter of the 2016 Chiloé earthquake was at 43.406°S, 73.941°W and 38 km deep with an origin time of 14:22:27 UTC [*NEIC*, 2016]. Teleseismic waves were used to rapidly determine the finite-fault slip distributions for the event [*NEIC*, 2016]. The best fitting nodal plane was oriented 4° NNW and had a dip angle of 16°. The estimated seismic moment release was 3.4×10^{20} Nm (M_w 7.6). The global centroid moment tensor (GCMT) solution indicated an almost pure double-couple faulting geometry with a 4° strike and 19° dip, at a centroid depth of 34.2 km, located at 43.41°S and 74.43°W. The centroid time shift was 11 s, and the seismic moment was 2.84×10^{20} Nm (M_w 7.5). The 2016 earthquake was followed by 24 $M > 4$ aftershocks within first 10 days, most of which occurred at shallower depths [*NEIC*, 2016]. These aftershocks were probably triggered by static Coulomb failure stress changes [*Tilmann et al.*, 2016] induced by the main shock or by aseismic creep [*Huang et al.*, 2017].

Interferometric synthetic aperture radar (InSAR) enables us to study megathrust earthquakes in Chile and has provided important information about the distribution of fault slips. *Tong et al.* [2010] captured the coseismic ground deformation of the 2010 M_w 8.8 Maule, Chile earthquake using Advanced Land Observatory Satellite data. The slip model shows an unevenly distributed along-strike fault slip and suggests that the maximum thrust slip of 17 m occurred at 120–160 km north of the epicenter. These data also enabled them to probe the downdip rupture limit of the seismogenic zone. Since the launch of Sentinel-1 in 2014, wide-swath imaging covering a region of up to 250 km has provided opportunities for InSAR to capture continent-wide deformation due to subduction megathrust earthquakes [*Solaro et al.*, 2016; *Xu et al.*, 2016]. The constellation of Sentinel-1A and Sentinel-1B further enables a 6 day satellite revisit time, thus significantly increasing the quality of InSAR products and improving our understanding of the seismic cycle [*Salvi et al.*, 2012]. *Grandin et al.* [2016] generated a complete three-dimensional coseismic ground deformation map associated with the 2015 M_w 8.3 Illapel earthquake by combining the Sentinel-1 data from different orbits. Here I first generate coseismic deformation maps associated with the 2016 M_w 7.5 Chiloé earthquake using sentinel-1 SAR
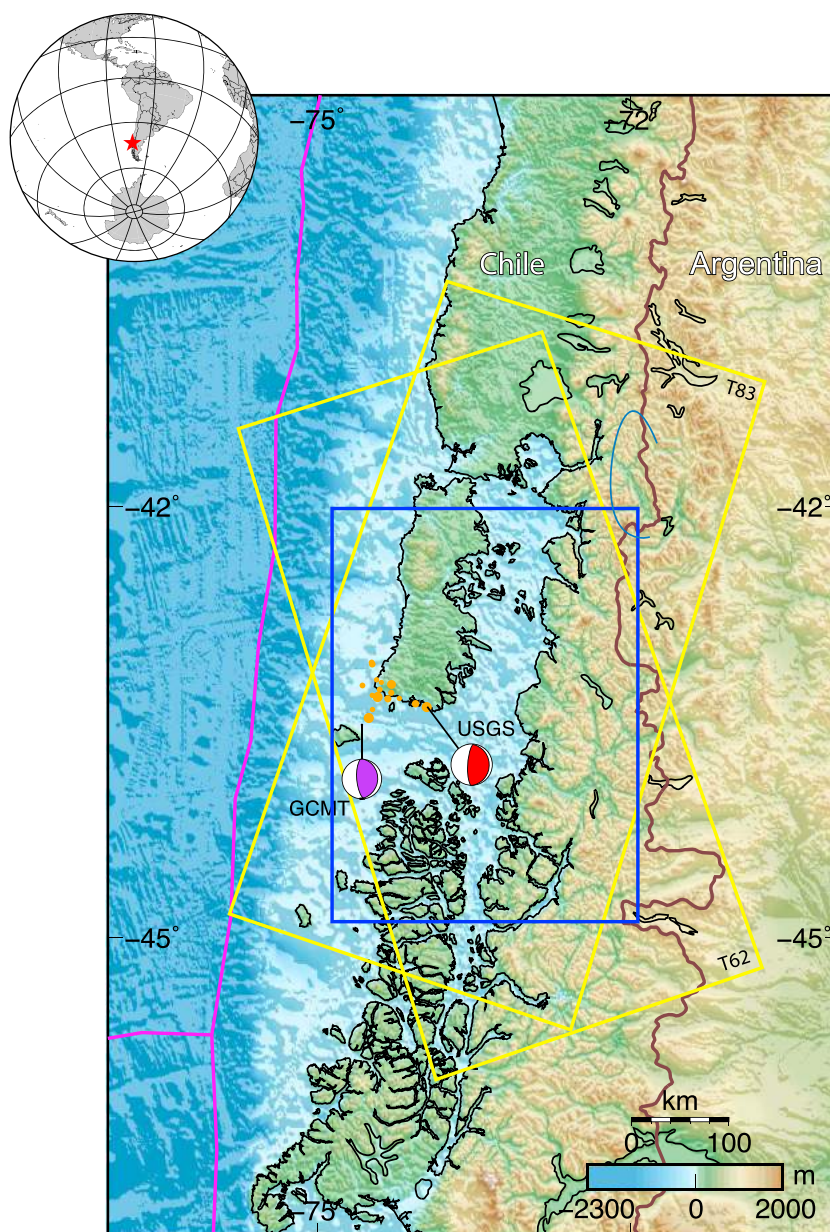
Figure 1. Location of the 2016 Chiloé earthquake in southern Chile. The orange dots represent the aftershocks recorded by the USGS, and the focal mechanisms indicate main shock locations from USGS (red) and GCMT (purple). The yellow boxes outline ascending and descending orbit SAR frames, respectively. The blue rectangle outlines the study area in the following figures. The magenta line marks the location of the trench.

data and range offsets from both ascending and descending orbits. Based on the observations, I search for the optimal fault geometry and invert for finite-fault slips. Finally, I discuss the implications and potential seismic hazards in the region.

2. Data Processing and Inversion Method

I generate coseismic interferograms from descending track 83 (17 December 2016 to 10 January 2017) and ascending track 62 (21 December 2016 to 14 January 2017) using Sentinel-1 C-band data in the Terrain Observations with Progressive Scans in azimuth (TOPS) mode (Table S1 in the supporting information). The interferogram of each track is mosaicked from three consecutive frames (Figure 1). I use Gamma software
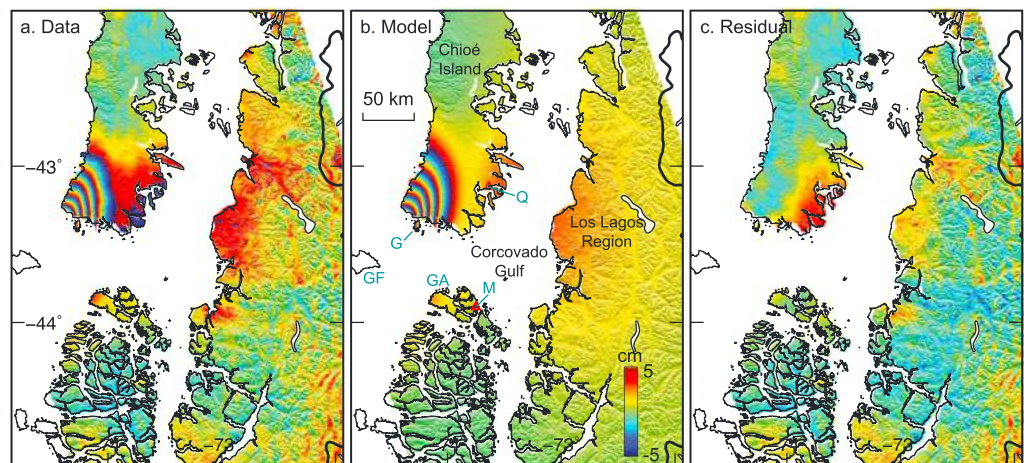
Figure 2. Coseismic InSAR data of the 2016 Chiloé earthquake and the modeling result. (a) Observed LOS displacement map from the ascending S1A satellite track 62. (b) Model prediction. (c) Residual. The interferogram is unwrapped and then rewrapped in this study. The scale is the same for all panels; one fringe corresponds to 10 cm line-of-sight (LOS) displacement. Major islands: GA, Guaitecas Archipelago; GF, Guafo; G, Guapiquilán. The red triangles represent the location of major cities: M, Melinka; Q, Quellón.

(http://www.gamma-rs.ch) and precise orbits provided by the European Space Agency to generate interferograms and range offsets. Image coregistration for TOPS mode SAR data is very important and requires extremely high accuracy. I first use precise orbits and the 30 m Shuttle Radar Topography Mission digital elevation model (SRTM DEM) to estimate terrain-induced pixel offsets [*Farr et al.*, 2007]. I then refine the coregistration using the amplitude matching procedure on the single look complex (SLC). I repeat this step until the azimuth offset correction is smaller than a 0.02 SLC pixel. Finally, I use a spectral diversity method that considers the double difference phase in the burst overlap regions to further improve the coregistration accuracy in the azimuth direction. Normally, after two or three iterations, the azimuth correction is reduced to 0.001 of a pixel. After the coregistration is done, I follow the standard two-pass InSAR data processing method [*Xu et al.*, 2016]. I simulate and eliminate topographic phase with the external SRTM DEM. I then unwrap interferograms with a minimum cost flow algorithm [*Chen and Zebker*, 2000]. The phase unwrapping near the epicenter is challenging due to intense ground deformation and loss of coherence, and isolated phases are seen on the Guaitecas Archipelago. I calculate range offsets from Sentinel-1 SLCs to help with phase unwrapping and retrieve deformation on Guafo island [*Michel et al.*, 1999]. The pixel spacing is 2.3 m in the range direction. Normally, this method can reach an accuracy of 0.1 pixel [*Michel et al.*, 1999]. The range offsets are nosier than in the InSAR data, but clear coseismic surface displacements can be seen in the range offsets on the southern part of Chiloé island and on Guafo island. With the guidance of range offsets, I manually check and adjust the incorrectly unwrapped phase by shifting an integer × 2π. I then geocode the unwrapped interferograms and range offset measurements into the World Geodetic System 84 coordinate system. Finally, I crop out the deformed area for further analysis (Figure 1).

I determine a finite-fault slip distribution model using the InSAR observations and range offset measurements from both ascending and descending orbits. I use a single rectangular dislocation [*Okada*, 1985] in a homogeneous and isotropic elastic Poisson half-space (Poisson's ratio v = 0.25). I subsample the data points using the quadtree method [*Jónsson et al.*, 2002] (Figure S1 in the supporting information). I fix the rake to 90° (pure thrust). I set bounds for the source parameters with the guidance from focal mechanism solutions (Table S2). I use the error variance to weight the data sets, assuming that they are independent in the modeling. A two-step nonlinear modeling approach is used to solve for the source parameters. I find the optimal fault model parameters with uniform thrust slip using a Monte Carlo-type simulated annealing algorithm, followed by a gradient-based iterative method using as initial guess the output from the simulated annealing [*Cervelli et al.*, 2001]. The optimal uniform slip model is 48 km long and 76 km wide with a strike angle of 4° and a dip angle of 27°. These estimated source parameters generally agree with the seismological solutions.
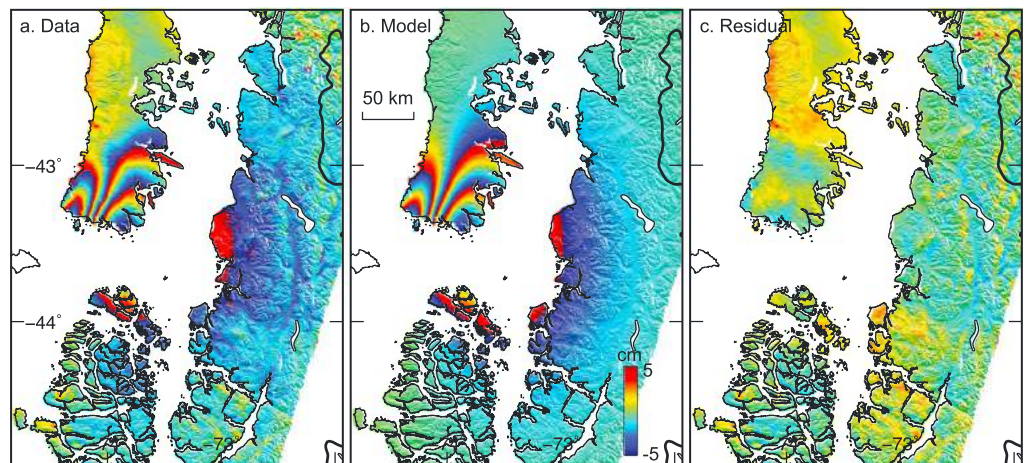
Figure 3. Same as Figure 2, but from the descending S1B satellite track 83.

To improve the fit of the model, I fix the model geometry and invert for finite-fault slip distribution using a linear least-squares inversion. I enlarge the fault to 100 km × 100 km and discretize the fault into small patches (5 km × 5 km). Laplacian smoothing is applied in the linear inversion to avoid abrupt variations in slip estimation. I find the best smoothing factor from the trade-off curve between the solution roughness and model fit to displacement (Figure S2).
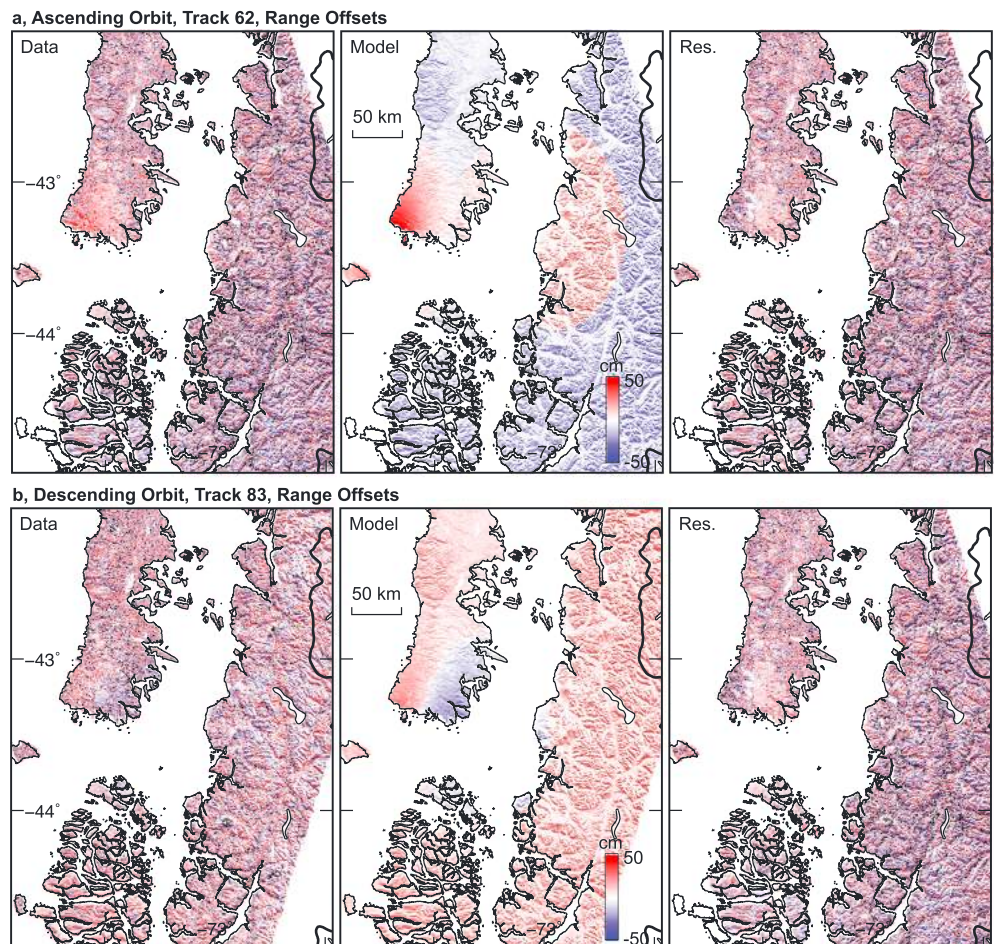

Figure 4. SAR image range offsets covering the epicenter area showing the LOS ground displacements.
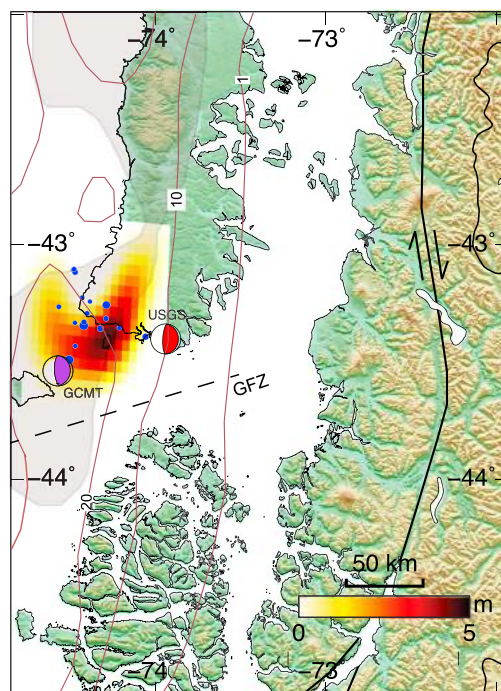
Figure 5. The spatial distribution of coseismic slip. (a) Slip distribution for a fault plane 100 km long, 100 km wide and dipping 27° east-southeast (see location in Figure 1), inverted from the ascending (Figure 2) and descending (Figure 3) InSAR data and range offsets. The focal mechanisms indicating main shock locations from NEIC (red) and GCMT (purple). The blue dots represent the aftershocks recorded by the USGS. The gray shaded area represents the region with locking rate over 0.75 [*Moreno et al.*, 2011]. The brown contours represent coseismic slip for the 1960 earthquake [*Moreno et al.*, 2009]. GFZ, Guafo Fracture Zone.

3. Results

The major coseismic deformation signals are confined to the southern side of the Chiloé island (Figures 2a and 3a). The maximum onshore displacement (~50 cm) in the radar line-of sight (LOS) direction is located approximately 60 km southwest of the city of Quellón. Both ascending and descending interferograms suggest that a significant portion of the displacement occurs offshore (Figures 2a and 3a). Ground deformation of about 5 cm in the LOS is also observed in the Guaitecas Archipelago and the Los Lagos region (Figures 2 and 3). The interferograms from different orbits produce different coseismic fringe patterns: the ascending interferogram shows up to five fringes (50 cm in LOS) close to the epicenter, while two lobes of fringes (20 cm in LOS) are seen on the descending interferogram. The different fringe patterns seen on the interferograms indicate that the horizontal displacement is as significant as the vertical motion of this event. The range offset measurements confirm that the LOS displacement reaches approximately 40 cm on Guafo island (Figure 4).

The finite fault slip distribution in Figure 5 shows that the fault's top edge is located at 10 km below sea level. The maximum slip (~4.7 m) from the preferred model is located at a depth of 35 km beneath Guapiquilán island. The predicted displacements fit the observations very well. The root-mean-square misfits of the best fitting model are 1.2, 87, 0.9, and 100 cm for the ascending InSAR data, range offsets, descending InSAR data, and range offsets, respectively. The residuals can be partly explained by unmolded offshore slip contributions, atmospheric artifacts, and the early postseismic deformation. Assuming that the shear modulus (μ) is 30 GPa, I calculate that the geodetic moment (M_0) is 2.4×10^{20} Nm, which is equivalent to M_w 7.56.

I examine the resolution of the slip distribution solutions through the checkerboard test (Figure S3) and the resolution matrix with three different smoothing factors (Figure S2). For a low smoothing weight, the fault slip is oscillatory with maximum slip up to 12 m, but for a higher value, the slip distribution is very smooth (Figure S2). Both checkerboard test and resolution matrix results suggest that InSAR data provide good resolution and inversion stability for downdip slip onshore but tend to underestimate and smear slip offshore.

4. Discussion and Conclusions

The modeling results indicate that the seismogenic zone is segmented in the updip direction. The 2016 event ruptured a region that was highly coupled between depths of about 15–45 km [*Moreno et al.*, 2011] (Figure 5). The downdip limit of the ruptured zone is spatially correlated with the coastal emergence and topography, which is compatible to similar magnitude earthquakes (e.g., 1997 Peru and 2007 *M*7.7 Tocopilla earthquakes) that have occurred in the Chilean subduction zone [*Pritchard et al.*, 2007; *Schurr et al.*, 2012]. The maximum fault slip is approximately 4.7 m, which is comparable with the results of the teleseismic inversions of

P and *SH* waves [*NEIC*, 2016]. The inverted focal depth (the peak slip location) is located beneath Guapiquilán island, where shallow higher coupling asperities transit to a deep lower coupling zone (Figure 5). The estimated dip angle (27°) is slightly larger than the 16° angle estimated by the USGS and the 19° angle estimated by GCMT but falls well within statistical analysis of similar earthquakes and is similar to previous findings at same latitude [*Linde and Silver*, 1989; *Bletery et al.*, 2016]. The total estimated geodetic moment (2.4×10^{20} Nm) is 71% of the NEIC value (3.4×10^{20} Nm) and 85% of the GCMT value (2.84×10^{20} Nm). The lower geodetic moment is likely due to the resolvability of InSAR data, which cannot provide good constraint for the offshore fault slip. The strain energy released by the asperity is calculated to be $\sim 1.1 \times 10^{23}$ J using the empirical equation $\log_{10} E = 1.5 M_w + 11.8$ [*Gutenberg and Richter*, 1955]. Based on the seismic moment and rupture area, the average stress drop ($\Delta\sigma$) of the asperity is estimated to be ~3.1 MPa using $\Delta\sigma = 2M_0/(\pi w^2 L)$ [*Kanamori and Anderson*, 1975], where w and L are the fault width and length, respectively. The value is compatible with the average stress-drop estimation of 3.4 MPa for $M_w \geq 7$ thrust-type earthquakes. According to Seno's hypothesis, the ruptured subduction zone segment is capable of producing $M_w \geq 9$ earthquakes [*Seno*, 2014]. Interseismic coupling model also suggests that the 1960 segment is highly locked and enough to produce an $M \sim 8$ event [*Moreno et al.*, 2011].

Multiple factors, including bathymetric features, sediment thickness, and plate complexity, have been invoked as controls on subduction earthquake nucleation, slip distribution, and termination [*Carena*, 2011; *Métois et al.*, 2012; *Bassett and Watts*, 2015]. The rupture plane of the 1960 Valdivia earthquake is limited by the Mocha Fracture Zone in the north and the Chile Rise in the south [*Moreno et al.*, 2009]. The main tectonic feature at the latitude where the 2016 event took place is the subducting Guafo Fracture Zone. Interestingly, the slip of the 2016 event is located north of the Guafo Fracture Zone and is arrested near the flank of this feature. The geometrical heterogeneity caused by the Guafo Fracture Zone may affect fluid pressure on the interface alternating the normal stress or modify the thermal regime forming a barrier [*Sparkes et al.*, 2010; *Wang and Bilek*, 2014]. These effects probably play an important role in controlling the 2016 earthquake rupture propagation.

Seismic activity has been unusually low on the 2016 M_w 7.5 Chiloé earthquake segment since the giant 1960 megathrust earthquake. Only eight $M > 4$ earthquakes occurred on the 2016 event segment, and none of them took place between 1961 and 2002 [*NEIC*, 2016]. This phenomenon is similar to the highly coupled Maule segment, at which very few moderate earthquakes occurred before the 2010 M_w 8.8 Maule earthquake [*Campos et al.*, 2002], and to the 2004 M_w 9.2 Sumatra earthquake, which also experienced a long period of seismic gap [*Lay*, 2015]. However, according to a recent study of a decade of continuous Global Positioning System data along the South American plate, *Melnick et al.* [2017] showed that the 2016 event was likely to be triggered by the 2010 Maule earthquake, which caused a superinterseismic phase of enhanced strain rates around the 2016 segment, bringing the fault closer to failure.

Nine $M_w \geq 7.5$ subduction earthquakes have occurred in the other sections along the South American subduction zone since 2000, including the Maule earthquake in south-central Chile (M_w 8.8 in 2010), the Iquique earthquake in northern Chile (M_w 8.2 in 2014), and the Illapel earthquake in central Chile (M_w 8.3 in 2015) [*Moreno et al.*, 2010; *Hayes et al.*, 2014; *Melgar et al.*, 2016]. These earthquakes generally ruptured within regions that were highly coupled during the interseismic period [*Métois et al.*, 2012]. It is believed that coseismic slips released or partly released accumulated elastic strain on these ruptured fault segments [*Moreno et al.*, 2010]. Considering that the Nazca plate is underthrusting the South America plate near the 2016 rupture at ~72 mm/yr [*DeMets et al.*, 2010], the slip deficit has been accumulated by approximately 4 m since the 1960 megathrust earthquake, assuming full coupling of the interface. The estimated coseismic peak slip of approximately 4.7 m in the 2016 event exceeds the deficits accumulated since the 1960 event, probably suggesting an earthquake supercycle behavior, as recently discovered in the Ecuadorian subduction zone [*Nocquet et al.*, 2017]. A large number of sections of the 1960 rupture zone remain unruptured and highly coupled [*Moreno et al.*, 2011]; as the elastic strain is accumulating, a significant seismic hazard remains for future great earthquakes in southern Chile.

References

Barrientos, S. E., and S. N. Ward (1990), The 1960 Chile earthquake: Inversion for slip distribution from surface deformation, *Geophys. J. Int.*, *103*, 589–598, doi:10.1111/j.1365-246X.1990.tb05673.x.

Bassett, D., and A. B. Watts (2015), Gravity anomalies, crustal structure, and seismicity at subduction zones: 1. Seafloor roughness and subducting relief, *Geochem. Geophys. Geosyst.*, *16*, 1508–1540, doi:10.1002/2014GC005684.

Bilek, S. L. (2010), Seismicity along the South American subduction zone: Review of large earthquakes, tsunamis, and subduction zone complexity, *Tectonophysics*, *495*, 2–14, doi:10.1016/j.tecto.2009.02.037.

Bletery, Q., A. M. Thomas, A. W. Rempel, L. Karlstrom, A. Sladen, and L. De Barros (2016), Mega-earthquakes rupture flat megathrusts, *Science*, *354*, 1027–1031, doi:10.1126/science.aag0482.

Campos, J., D. Hatzfeld, R. Madariaga, G. López, E. Kausel, A. Zollo, G. Iannacone, R. Fromm, S. Barrientos, and H. Lyon-Caen (2002), A seismological study of the 1835 seismic gap in south-central Chile, *Phys. Earth Planet. Inter.*, *132*, 177–195, doi:10.1016/S0031-9201(02)00051-1.

Carena, S. (2011), Subducting-plate topography and nucleation of great and giant earthquakes along the South American trench, *Seismol. Res. Lett.*, *82*, 629–637, doi:10.1785/gssrl.82.5.629.

Cervelli, P., M. H. Murray, P. Segall, Y. Aoki, and T. Kato (2001), Estimating source parameters from deformation data, with an application to the March 1997 earthquake swarm off the Izu Peninsula, Japan, *J. Geophys. Res.*, *106*, 11,217–11,237, doi:10.1029/2000JB900399.

Chen, C. W., and H. A. Zebker (2000), Network approaches to two-dimensional phase unwrapping: Intractability and two new algorithms, *J. Opt. Soc. Am.*, *17*, 401–414.

DeMets, C., R. G. Gordon, and D. F. Argus (2010), Geologically current plate motions, *Geophys. J. Int.*, *181*, 1–80, doi:10.1111/j.1365-246X.2009.04491.x.

Farr, T. G., et al. (2007), The shuttle radar topography mission, *Rev. Geophys.*, *45*, RG2004, doi:10.1029/2005RG000183.

Grandin, R., E. Klein, M. Métois, and C. Vigny (2016), Three-dimensional displacement field of the 2015 M_w8.3 Illapel earthquake (Chile) from across- and along-track Sentinel-1 TOPS interferometry, *Geophys. Res. Lett.*, *43*, 2552–2561, doi:10.1002/2016GL067954.

Gutenberg, B., and C. F. Richter (1955), Magnitude and energy of earthquakes, *Nature*, *176*, 795–795, doi:10.1038/176795a0.

Hayes, G. P., M. W. Herman, W. D. Barnhart, K. P. Furlong, S. Riquelme, H. Benz, E. Bergman, S. E. Barrientos, P. S. Earle, and S. V. Samsonov (2014), Continuing megathrust earthquake potential in Chile after the 2014 Iquique earthquake, *Nature*, *512*, 295–298, doi:10.1038/nature13677.

Huang, H., W. Xu, L. Meng, R. Bürgmann, and C. Baez (2017), Early aftershocks and afterslip surrounding the 2015 M_w 8.4 Illapel rupture, *Earth Planet. Sci. Lett.*, *457*, 282–291, doi:10.1016/j.epsl.2016.09.055.

Jónsson, S., H. Zebker, P. Segall, and F. Amelung (2002), Fault slip distribution of the 1999 M_w 7.1 Hector Mine, California, earthquake, estimated from satellite radar and GPS measurements, *Bull. Seismol. Soc. Am.*, *92*, 1377–1389.

Kanamori, H., and D. L. Anderson (1975), Theoretical basis of some empirical relations in seismology, *Bull. Seismol. Soc. Am.*, *65*, 1073–1095.

Lay, T. (2015), The surge of great earthquakes from 2004 to 2014, *Earth Planet. Sci. Lett.*, *409*, 133–146, doi:10.1016/j.epsl.2014.10.047.

Linde, A. T., and P. G. Silver (1989), Elevation changes and the great 1960 Chilean earthquake: Support for aseismic slip, *Geophys. Res. Lett.*, *16*, 1305–1308, doi:10.1029/GL016i011p01305.

Melgar, D., W. Fan, S. Riquelme, J. Geng, C. Liang, M. Fuentes, G. Vargas, R. M. Allen, P. M. Shearer, and E. J. Fielding (2016), Slip segmentation and slow rupture to the trench during the 2015, M_w8.3 Illapel, Chile earthquake, *Geophys. Res. Lett.*, *43*, 961–966, doi:10.1002/2015GL067369.

Melnick, D., M. Moreno, J. Quinteros, J. C. Baez, Z. Deng, S. Li, and O. Oncken (2017), The super-interseismic phase of the megathrust earthquake cycle in Chile, *Geophys. Res. Lett.*, *44*, 784–791, doi:10.1002/2016GL071845.

Métois, M., A. Socquet, and C. Vigny (2012), Interseismic coupling, segmentation and mechanical behavior of the central Chile subduction zone, *J. Geophys. Res.*, *117*, B03406, doi:10.1029/2011JB008736.

Michel, R., J. P. Avouac, and J. Taboury (1999), Measuring ground displacements from SAR amplitude images: Application to the Landers earthquake, *Geophys. Res. Lett.*, *26*, 875–878, doi:10.1029/1999GL900138.

Moreno, M., et al. (2011), Heterogeneous plate locking in the south-central Chile subduction zone: Building up the next great earthquake, *Earth Planet. Sci. Lett.*, *305*, 413–424, doi:10.1016/j.epsl.2011.03.025.

Moreno, M., M. Rosenau, and O. Oncken (2010), Maule earthquake slip correlates with pre-seismic locking of Andean subduction zone, *Nature*, *467*, 198–202, doi:10.1038/nature09349.

Moreno, M. S., J. Bolte, J. Klotz, and D. Melnick (2009), Impact of megathrust geometry on inversion of coseismic slip from geodetic data: Application to the 1960 Chile earthquake, *Geophys. Res. Lett.*, *36*, L16310, doi:10.1029/2009GL039276.

National Earthquake Information Center (NEIC) (2016), *M7.6 41 km SW of Puerto Quellon, Chile*, U.S. Geol. Surv., Denver, Colo. [Available at https://earthquake.usgs.gov/earthquakes/eventpage/us10007mn3#finite-fault.]

Nocquet, J. M., et al. (2017), Supercycle at the Ecuadorian subduction zone revealed after the 2016 Pedernales earthquake, *Nat. Geosci.*, *10*, 145–149, doi:10.1038/ngeo2864.

Okada, Y. (1985), Surface deformation due to shear and tensile faults in a half-space, *Bull. Seismol. Soc. Am.*, *75*, 1135–1154.

Pritchard, M. E., E. O. Norabuena, C. Ji, R. Boroschek, D. Comte, M. Simons, T. H. Dixon, and P. A. Rosen (2007), Geodetic, teleseismic, and strong motion constraints on slip from recent southern Peru subduction zone earthquakes, *J. Geophys. Res.*, *112*, B03307, doi:10.1029/2006JB004294.

Salvi, S., S. Stramondo, G. J. Funning, A. Ferretti, F. Sarti, and A. Mouratidis (2012), The Sentinel-1 mission for the improvement of the scientific understanding and the operational monitoring of the seismic cycle, *Remote Sens. Environ.*, *120*, 164–174, doi:10.1016/j.rse.2011.09.029.

Seno, T. (2014), Stress drop as a criterion to differentiate subduction zones where M_w 9 earthquakes can occur, *Tectonophysics*, *621*, 198–210, doi:10.1016/j.tecto.2014.02.016.

Schurr, B., G. Asch, M. Rosenau, R. Wang, O. Oncken, S. Barrientos, P. Salazar, and J.-P. Vilotte (2012), The 2007 *M7.7* Tocopilla northern Chile earthquake sequence: Implications for along-strike and downdip rupture segmentation and megathrust frictional behavior, *J. Geophys. Res.*, *117*, B05305, doi:10.1029/2011JB009030.

Solaro G., V. De Novellis, R. Castaldo, C. De Luca, R. Lanari, M. Manunta, and F. Casu (2016), Coseismic fault model of M_w 8.3 2015 Illapel earthquake (Chile) retrieved from multi-orbit Sentinel1-A DInSAR measurements, *Remote Sens.*, *8*(4), 323, doi:10.3390/rs8040323.

Sparkes, R., F. Tilmann, N. Hovius, and J. Hillier (2010), Subducted seafloor relief stops rupture in South American great earthquakes: Implications for rupture behaviour in the 2010 Maule, Chile earthquake, *Earth Planet. Sci. Lett.*, *298*, 89–94, doi:10.1016/j.epsl.2010.07.029.

Tilmann, F., et al. (2016), The 2015 Illapel earthquake, central Chile: A type case for a characteristic earthquake?, *Geophys. Res. Lett.*, *43*, 574–583, doi:10.1002/2015GL066963.

Tong, X., et al. (2010), The 2010 Maule, Chile earthquake: Downdip rupture limit revealed by space geodesy, *Geophys. Res. Lett.*, *37*, L24311, doi:10.1029/2010GL045805.

Wang, K., and S. L. Bilek (2014), Invited review paper: Fault creep caused by subduction of rough seafloor relief, *Tectonophysics*, *610*, 1–24, doi:10.1016/j.tecto.2013.11.024.

Xu, B., Z. Li, G. Feng, Z. Zhang, Q. Wang, J. Hu, and X. Chen (2016), Continent-wide 2-D co-seismic deformation of the 2015 M_w 8.3 Illapel, Chile earthquake derived from Sentinel-1A data: Correction of azimuth co-registration error, *Remote Sens.*, *8*(5), 376, doi:10.3390/rs8050376.

Xu, W., S. Jónsson, J. Ruch, and Y. Aoki (2016), The 2015 Wolf volcano (Galápagos) eruption studied using Sentinel-1 and ALOS-2 data, *Geophys. Res. Lett.*, *43*, 9573–9580, doi:10.1002/2016GL069820.